Available online at www.sciencedirect.com
ScienceDirect
Trans. Nonferrous Met. Soc. China 35(2025) 1543−1559
Transactions of Nonferrous Metals Society of China
www.tnmsc.cn

Phase selection prediction and component determination of multiple-principal amorphous alloy composites based on artificial neural network model

Lin WANG[1], Pei-you LI[1], Wei ZHANG[1], Xiao-ling FU[2],
Fang-yi WAN[3], Yong-shan WANG[1], Lin-sen SHU[4], Long-quan YONG[5]

1. School of Materials Science and Engineering, Shaanxi University of Technology, Hanzhong 723001, China;
2. School of Materials and Energy, Guangdong University of Technology, Guangzhou 510006, China;
3. School of Aeronautics, Northwestern Polytechnical University, Xi'an 710071, China;
4. School of Mechanical Engineering, Shaanxi University of Technology, Hanzhong 723001, China;
5. School of Mathematics and Computer Science, Shaanxi University of Technology, Hanzhong 723001, China

Received 7 September 2023; accepted 21 May 2024

Abstract: The probability of phase formation was predicted using *k*-nearest neighbor algorithm (KNN) and artificial neural network algorithm (ANN). Additionally, the composition ranges of Ti, Cu, Ni, and Hf in 40 unknown amorphous alloy composites (AACs) were predicted using ANN. The predicted alloys were then experimentally verified through X-ray diffraction (XRD) and high-resolution transmission electron microscopy (HRTEM). The prediction accuracies of the ANN for AM and IM phases are 93.12% and 85.16%, respectively, while the prediction accuracies of KNN for AM and IM phases are 93% and 84%, respectively. It is observed that when the contents of Ti, Cu, Ni, and Hf fall within the ranges of 32.7−34.5 at.%, 16.4−17.3 at.%, 30.9−32.7 at.%, and 17.3−18.3 at.%, respectively, it is more likely to form AACs. Based on the results of XRD and HRTEM, the $Ti_{34}Cu_{17}Ni_{31.36}Hf_{17.64}$ and $Ti_{36}Cu_{18}Ni_{29.44}Hf_{16.56}$ alloys are identified as good AACs, which are in closely consistent with the predicted amorphous alloy compositions.

Key words: multiple-principal amorphous alloy composites; Ti−Cu−Ni−Hf alloy; phase selection; artificial neural network; machine learning

1 Introduction

Intelligent machine learning involves training a flexible and highly nonlinear model based on available data. It is particularly useful for handling the complex relationship among the material composition, phase structure, and performance, which may be challenging to address using traditional methods based on physical principles. As a result, intelligent machine learning has emerged a valuable tool for predicting material performance, screening, and optimizing component design [1−5]. In the context of predicting phase selection in multi-principal component alloys, ISLAM et al [6] achieved a remarkable prediction accuracy of 99.2% using a neural network model. However, the accuracy of phase prediction in alloys will vary depending on the specific algorithms used. For instance, HOU et al [7] integrated empirical knowledge models into the prediction process, leading to prediction accuracies exceeding 83.3%.

Among the 13 feature parameter selections, different parameter combinations yield varying accuracies in predicting the phases of high-entropy alloys (HEAs). ZHOU et al [8] reported prediction

Corresponding author: Pei-you LI, Tel: +86-15891629301, E-mail: lipeiyou112@163.com
https://doi.org/10.1016/S1003-6326(25)66766-5

accuracies of 98.9%, 95.6%, and 97.8% for AM, IM, and SS phases, respectively, using an artificial neural network (ANN) model. They also emphasized the importance of feature parameters based on potential−energy distribution function (PEL) in phase prediction. Therefore, machine learning exhibits high accuracy in phase selection for multi-principal component alloys and HEAs. However, when it comes to predicting the optimal performance of the alloy components, LI et al [9] proposed a data-driven approach to expedite the design of magnetic HEAs that combine saturation magnetization (M_s) and hardness (H). They developed a multi-objective optimization algorithm to search for the optimal alloy composition. The support vector regression (SVR) model achieved the smallest root mean square error (RMSE) of 13.9 A·m^2/kg for magnetization prediction, while the LightGBM model attained the smallest RMSE value of HV 57.6 for hardness prediction.

The selection of feature parameters is a crucial aspect in both phase selection and performance prediction of alloys. It is essential to strike a balance between the number of selected feature parameters, as a small number may result in decreased prediction accuracy while too many can make the prediction process cumbersome. LI et al [10] proposed an effective approach for reducing the number of feature parameter selection without sacrificing accuracy. They employed five models to predict magnetic performance (B_s) and maximum critical size (D_{max}). The XGBoost model achieved an impressive R^2 value of 0.93 for predicting B_s and 0.68 for predicting D_{max}. The results demonstrate that machine learning exhibits excellent generalization performance in the field of phase selection and performance prediction of alloys.

Intelligent machine learning has been proven to be highly effective in predicting the composition and glass-forming ability of multi-principal amorphous alloys (AMs) [11]. Additionally, it can also predict key parameters that influence the larger casting diameter of amorphous alloys [11], and even facilitate the prediction and design ultra-high strength multi-principal alloys [12]. This demonstrates that intelligent machine learning is a powerful method for predicting the composition, structure, and performance of multi-principal alloys. Several regression algorithms, including Gaussian process regression [13], ANN [14] and support vector machine (SVM) [15], are commonly employed in this field. Among them, the ANN model has shown high accuracy in predicting phase selection for multi-principal alloys, with the atomic size difference (δ) playing a significant role in this process [16−18]. To predict the phase selection of AM, IM and SS phases, previous research showed that a combination of three parameters, namely, standard deviation of electronegativity ($\Delta\chi$), ideal mixing entropy (S_{id}) and δ, yields higher prediction accuracy (P_c) compared to a combination of four parameters, including δ, $\Delta\chi$, average enthalpy change of mixing (ΔH_m) and S_{id} [19]. Based on this finding, the present study utilized the three-parameter combination (δ, $\Delta\chi$ and S_{id}) to predict the phase selection in amorphous alloy composites (AACs). By employing intelligent machine techniques, this approach enables rapid exploration and establishment of relationships between the alloy components and phases. Consequently, it offers valuable insights for the further development of multi-principal AACs by providing predictions regarding composition ranges and phase selections.

2 Data and models

2.1 Selected data

In Table S1 of Supplementary Materials, the compositional phases (110 AM, 110 SS, and 110 IM phases) and the values of three parameters (δ, $\Delta\chi$ and S_{id}) for 330 alloys are listed [6]. For both the KNN and ANN models, these 330 data points are randomly divided into training and testing sets in an 8:2 ratio, meaning that 80% of the data is used for training and 20% for testing.

2.2 KNN model

One simple approach to determine the category of a sample is to directly compare its similarity with the category of training samples and classify it as the one with the highest similarity. The KNN algorithm was first proposed by COVER and HART in 1967 [20]. Its core idea is to select the k sample attributes that are closest to those of the experimental and training samples and consider them as a set. Then, through voting, the category with the highest number of attributes from this set is determined as the final predicted category for the sample. In the KNN algorithm, similarity is

quantified using distance (d), which is typically calculated using the Euclidean distance formula as follows [21]:

$$d(x,y)=\sqrt{\sum_{i=1}^{n}(x_i-y_i)^2} \tag{1}$$

where x_i and y_i represent the known coordinates of two points, respectively, and $d(x, y)$ represents the distance between these two points.

2.3 ANN model

Artificial neurons serve as the fundamental units of information processing, existing between different layers in a neural network. These layers typically include an input layer, a hidden layer, and an output layer. The hidden layer comprises multiple layers, rather than just a single one. In this study, the backpropagation (BP) ANN algorithm is employed for data processing and prediction. The BP neural network, originally proposed by RUMELHART and MCCLELLAND [22] in 1987, is a type of unidirectional, multi-layer feedforward neural network. In the hierarchical structure of multi-layer feedforward neural networks, each layer of neurons establishes connections with the next layer through complete interconnection. There are no connections between different neurons in the same layer, nor can a certain layer skip and make cross-layer connections with the next layer. By repeatedly fitting simple nonlinear functions multiple times, the BP neural network can approximate complex nonlinear functions. Thus, the BP neural network performs a highly nonlinear mapping process from the input to the output. In this process, an artificial neuron consists of a linear model and an activation function. The expression for the linear model is as follows [23]:

$$y=f(\boldsymbol{\omega}^{\mathrm{T}}\boldsymbol{x}+\boldsymbol{b}) \tag{2}$$

where $\boldsymbol{x}$ refers to the input vector; $\boldsymbol{\omega}$ represents the weight vector, which generally reflects the importance of input values to output categories (A larger $\boldsymbol{\omega}$ value indicates a greater proportion of input parameters in output characteristics); T stands for transpose matrix; $\boldsymbol{b}$ refers to the deviation term vector. ANNs establish connections between input and output layers primarily through weights and bias terms. When the hidden layer is multi-layer, the output values from the previous layer are used as new input values through the generalization effect of the model to generate new output values. The $\boldsymbol{\omega}$ and $\boldsymbol{b}$ reveal the fundamental principles of ANNs, making them crucial parameters to consider in machine learning.

The reason why ANN model can be connected into a nonlinear model is the essential role played by nonlinear activation functions. In BP neural networks, a commonly used activation function is represented by the sigmoid function $\sigma(x)$, which is expressed as [16]

$$\sigma(x)=\frac{1}{1+\mathrm{e}^{-x}} \tag{3}$$

The sigmoid function can transform an ANN model into a nonlinear model by introducing nonlinear elements. The expression of the sigmoid function ensures that the output values of the model are confined within the range of [0,1]. This characteristic allows the model to capture and represent nonlinear relationships in the data. Compared to linear models, nonlinear models have better generalization performance.

The basic working principle of neural networks can be roughly explained from two aspects. Firstly, when the potential changes caused by "excited" neurons exceed a specific "threshold" the neurons will be activated. Secondly, according to Eq. (2), each iteration multiplies the initial input value by a certain $\boldsymbol{\omega}$ and adds other input values to the neuron queue. The processed neurons are then adjusted using $\boldsymbol{b}$ and the output values are uniformly normalized. By continuously adjusting $\boldsymbol{\omega}$ and $\boldsymbol{b}$ through the same operation, the final output value approaches the actual result. Normalization processing is typically carried out as follows:

$$x'=\frac{x-x_{\min}}{x_{\max}-x_{\min}} \tag{4}$$

where x' is the normalized input value, x represents the input value, $x_{\min}$ represents the minimum value among the input values, and $x_{\max}$ represents the maximum value among the input values. The purpose of normalization is to transform the input values into a common range of [0,1].

2.4 Experimental procedure

The Ti−Cu−Ni−Zr−Hf and Ti−Cu−Ni−Hf alloy ingots weigh 20 g each. Each raw material alloy is in block shape and has a purity greater than 99.9%. The process begins by placing 20 g of alloy

raw materials into a water-cooled copper crucible in a vacuum melting furnace for melting. High-purity argon is used as the protective gas during the smelting process. Each alloy ingot is melted four times to ensure uniformity in the chemical composition of the alloy ingot. After melting, the molten alloy is transferred to a suction casting crucible and remelted. It is then cast into a water-cooled copper mold to form cylindrical rods with a diameter of 3 mm and a length of 50 mm. The phase composition of the alloys is characterized using X-ray diffraction (XRD) with Cu K_α radiation at a voltage of 30 kV. To further analyze the alloys, high-resolution images are observed using a high-resolution transmission electron microscope (HRTEM) with an operating voltage of 200 kV and a JEM−2100F instrument. Thin samples for HRTEM observation are prepared using the electrolytic double-spray thinning method in an electrolyte solution consisting of 25 vol.% HNO_3 and 75 vol.% methanol at approximately 238 K.

3 Results and discussion

3.1 Phase-selection prediction using *k*-nearest neighbor algorithm

Determining the value of parameter k is crucial in the KNN algorithm as it directly impacts the fitting effect of the model on the data, thereby influencing the prediction accuracy (P_c). One effective method to obtain the optimal k-value in KNN is through k-fold cross-validation. The process of k-fold cross-validation involves dividing the dataset into k segments. Each segment is then further divided into training and testing sets. The KNN model is trained on each segment to calculate the average P_c for each model. By comparing the average P_c values, the k-value with the highest average P_c is selected as the optimal value. This iterative process ensures that the selected k-value leads to the best overall prediction accuracy. To evaluate performance of different k-fold cross-validation methods, the predictions of AM phase and IM phase were performed on 330 data. Figure 1 illustrates the average P_c of AM, IM, and SS phases for the 15 predictions using various k values. Additionally, it depicts the correlation coefficient values (R) obtained from cross-validation with different numbers of folds.

In Fig. 1(a), the prediction accuracy of three types of alloy phases increases as the k values change from 1 to 5. However, when the k values are within the range from 5 to 10, the prediction accuracy decreases with an increase in the k value. In fact, a smaller value of k indicates a lower P_c value. This is due to the lack of training data, leading to underfitting of the model. On the other hand, a larger value of k results in lower prediction accuracy. This is because samples that are farther away from the target sample in the KNN model contribute to prediction errors. Therefore, selecting an appropriate value of k is crucial for achieving higher prediction accuracy. When k=5 is chosen, the P_c(AM) value is 92.9%. The highest values for P_c(IM) and P_c(SS) are 84.1% and 89.2% respectively. To assess the accuracy of the model, a correlation coefficient R is used in conjunction with statistical indicators.

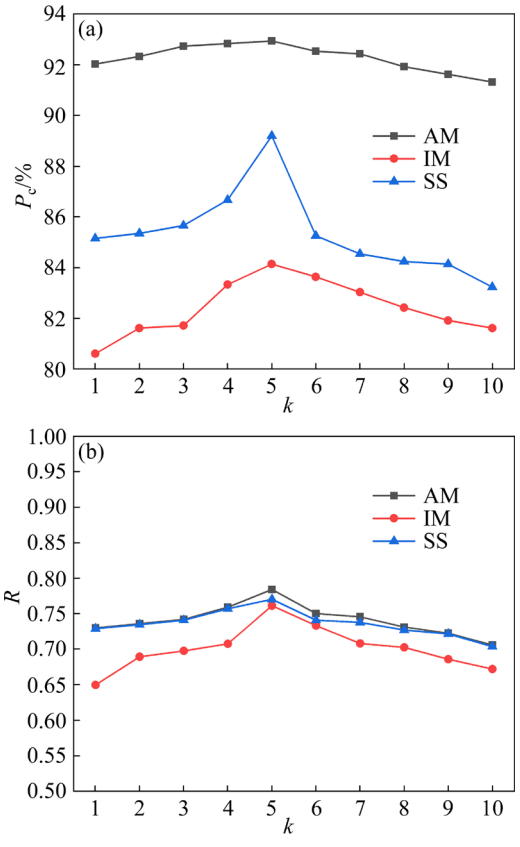

Fig. 1 Average prediction accuracies (P_c) (a) and correlation coefficient (R) (b) for AM, IM, and SS phases predicted under different k values in k-fold cross-validation of KNN algorithm

In Fig. 1(b), both the correlation coefficient and prediction accuracy exhibit the same trend of change. Additionally, the R value of the AM phase

is higher than that of the IM and SS phases, and the prediction accuracy of the AM phase is also higher compared to the IM and SS phases. When the R value is larger, there is a corresponding increase in the prediction accuracy, indicating that the current KNN model accurately predicts the phase selection of the three types of alloys under different k values.

When k is equal to 5, Fig. 2 displays the prediction accuracies, mean squared error (MSE), and R values of the KNN algorithm for the selection of AM, IM, and SS phases. A smaller MSE value indicates a larger P_c value for phase selection. The phase selection of AM phase exhibits a smaller MSE value, while the phase selection of IM phase shows a larger MSE value. These results suggest that the current model achieves a higher P_c value for AM phase selection, but a lower P_c value for IM phase selection.

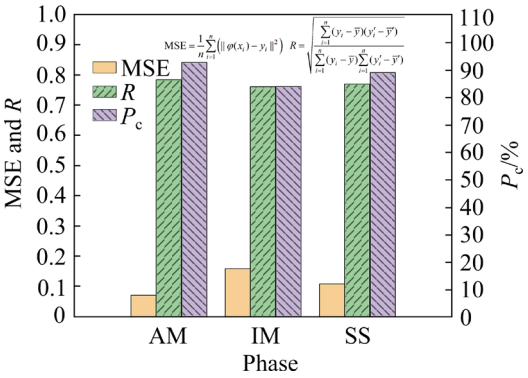

Fig. 2 P_c, MSE, and R values of KNN algorithm (k=5) for phase selection in AM, IM, and SS phase

In the KNN phase-selection regression algorithm, the k training samples are selected and the distances are calculated between these k points and the sample points to be predicted. Finally, the category is chosen to which most of the neighboring training sample points belong to the output category for predicting unknown sample points. Therefore, the predicted output value for phase selection of each alloy can only be 0 or 1, representing negative or positive examples. In the regression algorithm for phase selection in SVM, the prediction accuracy for the AM and IM phases is 94% and 85.4%, respectively. The predicted output values for phase selection of each alloy are also either 0 or 1 [24]. However, in the ANN phase-selection regression algorithm, the output values for AM phase selection in Ti−Cu−Ni−Zr amorphous alloys are continuous values close to 1 [19]. This is because in the ANN algorithm, the predicted output values need to be normalized, resulting in continuous values between 0 and 1. In order to predict the phase selection of AACs, machine learning algorithms should generate continuous values close to 1 when selecting AM and IM phases. Therefore, both the ANN and KNN models can be utilized for predicting the phase composition of AACs. However, in terms of prediction accuracy P_c, R, and MSE values, the ANN model exhibits more advantages compared to the KNN model.

3.2 Phase selection prediction in AM and IM phases using ANN algorithm

For the 110 AMs (amorphous high-entropy alloys), 110 SSs (solid solution high-entropy alloys), and 110 IMs (high-entropy alloys containing intermetallic compounds), a well-performing ANN model can be designed. The model consists of one input layer, one hidden layer, and one output layer, with 3 nodes in the input layer, 10 nodes in the hidden layer, and 1 node in the output layer. Due to the small size of the selected dataset (330 samples), choosing an ANN with one hidden layer demonstrates better prediction accuracy and generalization performance compared to a multi-layer deep neural network. This decision is made considering the characteristics of the available data and the complexity involved in training the model [19]. Using a hidden layer in this work will yield the improved prediction results. The number of nodes in the hidden layer is also a crucial factor to consider. Different numbers of nodes in the hidden layer will lead to varying levels of prediction accuracy, making it necessary to determine the optimal number through testing. According to the results of 15 tests of 30 AM alloys presented in Table S2 in Supplementary Materials, it was found that the prediction accuracy and generalization performance are optimal when the hidden layer contains 10 nodes.

Figure 3 illustrates the average P_c, R and MSE values for the AM and IM phase selections. The findings indicate that in the prediction of the AM phase for 330 alloys, the average P_c value for the 15 test sets using three parameter combinations of $\delta + \Delta\chi + S_{id}$ is 93.12%. This value is slightly lower than the average P_c value (94.5%) reported in Ref. [19] for the same three parameter combinations.

However, the current learning model still demonstrates a high P_c value for this dataset. On the other hand, in the prediction of the IM phase selection, the P_c value for the test set of 330 alloys is 85.16%. Therefore, the current model exhibits higher P_c(AM) values and lower P_c(IM) values.

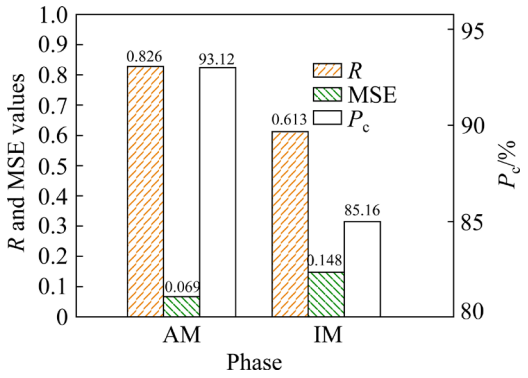

Fig. 3 P_c, R and MSE values of 330 alloys in AM and IM phase predictions using ANN model

In Fig. 3, the larger the R value, the higher the P_c value. The R(AM) value is 0.826, while the R(IM) value is 0.613, indicating that the P_c(AM) value is greater than the P_c(IM) value. A smaller MSE value indicates that the predicted value is closer to the true value, and also corresponds to a higher P_c value. The AM phase selection yields a predicted MSE value of 0.069 for 330 alloys, which is smaller than the MSE value obtained with IM phase selection (0.148). This suggests that the model has a higher P_c(AM) value and a lower P_c(IM) value.

In an ANN model, as the threshold of each alloy unit approaches 1, the phase composition of the alloy gets closer to the true value and the neuronal activation level increases. Conversely, when the threshold of each alloy unit approaches 0, the true value of the alloy's phase composition will be suppressed. In the case of predicting phase selection for the 330 alloys, only 15 predicted values are obtained for phase selection, and the specific threshold for each alloy unit is unknown. When the threshold of an alloy unit approaches 1, the predicted phase becomes closer to the actual phase, indicating a higher P_c value for the alloy's phase selection. During each prediction, an alloy will have a threshold. By summing the absolute values of the 15 predicted thresholds, the sum of these 15 predicted values is obtained, as shown in Fig. 4(a). When the predicted value is greater than 0.5, it indicates a positive example for the phase selection of the alloy. Conversely, when the predicted value is less than 0.5, it represents a negative example. If the real category matches the predicted category, it is represented as "true"; if they are different, it is represented as "false".

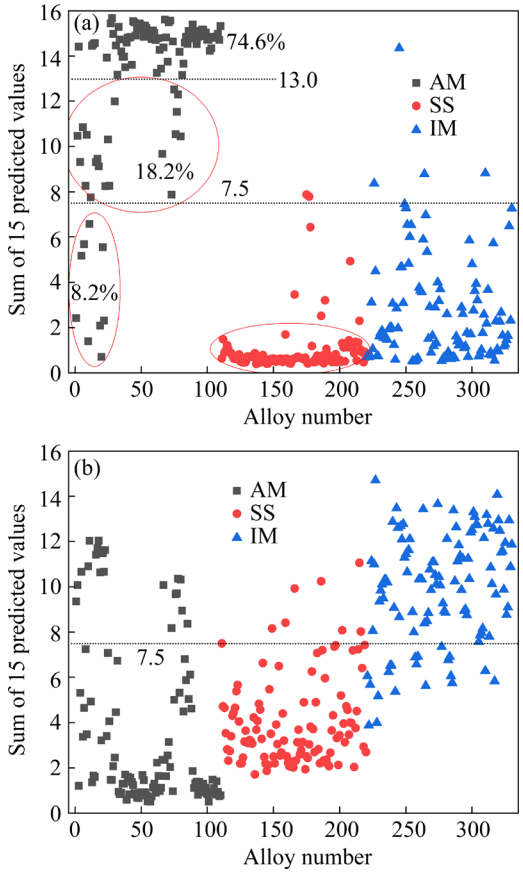

Fig. 4 Sum of 15 predicted values for AM (a) and IM (b) phases in 330 alloys

In the prediction of AM phase selection for 110 AM alloys, it was found that for 9 alloys, the total of their 15 predicted values is less than 7.5. This indicates that these 9 alloys are false negative examples, meaning that their actual AM phase was not correctly predicted. On the other hand, when the sum of the 15 predicted values fluctuates around 15, it suggests a higher degree of neural activation, indicating a closer proximity of the predicted AM phase to the real AM phase of the alloy. Regarding the prediction of the AM phase for 110 SS and 110 IM alloys, only a small number of these alloys have predicted values greater than 7.5. This suggests that the phase prediction for these particular alloys is prone to false positives, meaning that their predicted AM phase does not align with the actual phase of the alloy. False negative and false positive examples have an impact on the P_c value of phase

selection in AM alloys. In Fig. 4(b), for the prediction of IM phase selection, the sum of 15 predicted values for certain AM and SS phases exceeds 7.5, resulting in more false positive samples. Conversely, for some IM alloys, the sum of 15 predicted values falls below 7.5, leading to more false negative samples. The presence of a high number of false positive and false negative examples contributes to a lower P_c value for phase selection in IM alloys.

In Fig. 4(a), it is observed that 15 predicted values of AM alloys, representing 18.2% of the total, fall within the range of 7.5 to 13.0. Although these predictions correctly identify the alloys as positive examples, a notable discrepancy exists between this range and the total number of 15 alloys. This suggests that the AM alloys within the 18.2% group exhibit a weaker activation of neurons in AM phase-selection prediction compared to the AM alloys belonging to the 74.6% group. Consequently, this indicates a lower probability of these 21 AM alloys forming amorphous structures. To further investigate these 21 alloys, their respective 15 predicted values for AM and IM phase selection are included in Table 1 and visually represented in Fig. 5.

In Fig. 5, the aggregation of the 15 predicted values for the 10 alloys in the IM phase prediction surpasses the threshold of 7.5. This observation suggests that these 10 alloys are falsely identified as positive examples in the prediction of the IM phase. Despite this, their high predicted values also indicate a relatively high level of neuronal activation during the formation of the IM phase. In essence, these 10 alloys display a noteworthy neural activation when it comes to selecting both AM and IM phases. This implies that these alloys have the potential to form amorphous composites containing a mixture of amorphous and crystalline structures.

In the context of model learning, the aggregation of 15 predicted values for the $Zr_{17}Ta_{16}Ti_{19}Nb_{22}Si_{26}$ alloy, when considering both the AM and IM phase selections, exceeds the threshold of 7.5, reaching 10.47 and 10.08, respectively. Notably, in the absence of the Si element, the quaternary Zr−Ta−Ti−Nb alloy system exhibits a propensity to form solid solution alloys [25]. However, to favor the emergence of amorphous structures, a significant quantity of Si is incorporated into the alloy, aiming to establish a eutectic structure alongside the other four constituent elements. Numerous eutectic clusters are present within the alloy solution, which becomes advantageous for an amorphous structure

Table 1 Sum of 15 predicted values for 21 AM alloys (P_{am} and P_{im}) in AM and IM phase selection, and experimental (Exp.) and predicted (Pre.) phases

Alloy	P_{am}	P_{im}	Exp.	Pre.
$Zr_{17}Ta_{16}Ti_{19}Nb_{22}Si_{26}$	10.47	10.08	AM	AM+IM
$Ni_{50}Nb_{50}$	9.31	5.31	AM	AM
SrCaYbMgZn	10.85	3.37	AM	AM
SrCaYbMgZnCu	8.17	4.65	AM	AM
SrCaYbLi0.55Mg0.45Zn	8.26	7.24	AM	AM
ErTbDyNiAl	10.51	3.48	AM	AM
$Pd_{75}Si_{25}$	7.76	0.11	AM	AM
ZrHfTiCuNi	9.31	11.41	AM	AM+IM
ZrHfTiCuFe	9.46	11.71	AM	AM+IM
ZrHfTiCuCo	9.12	12.04	AM	AM+IM
AlMoNbSiTaTiVZr	8.25	11.63	AM	AM+IM
$Pd_{40}Cu_{30}Ni_{10}P_{20}$	10.31	7.08	AM	AM
$Fe_{41}Co_7Cr_{15}Mo_{14}C_{15}B_6Y_2$	8.26	4.06	AM	AM
$Co_{48}Cr_{15}Mo_{14}C_{15}B_6Er_2$	12.00	2.46	AM	AM
$Mg_{80}Ni_{10}Nd_{10}$	9.68	2.36	AM	AM
$Pd_{77}Si_{17}Cu_6$	7.88	8.17	AM	AM+IM
$Pd_{40}Ni_{40}P_{20}$	12.52	5.01	AM	AM
$Ti_{40}Cu_{32}Pd_{18}Zr_{10}$	10.55	9.67	AM	AM+IM
$Ti_{40}Cu_{36}Pd_{14}Zr_{10}$	11.53	9.71	AM	AM+IM
$Ti_{40}Cu_{40}Pd_{10}Zr_{10}$	12.30	10.35	AM	AM+IM
$Ti_{50}Cu_{32}Ni_{30}Sn_3$	10.44	10.32	AM	AM+IM

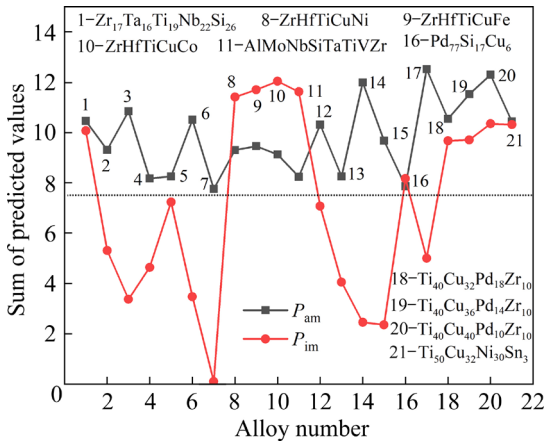

Fig. 5 Sum of 15 predicted values (P_{am} and P_{im}) for 21 AM alloys in AM and IM phase selection

to form at a particular cooling rate. In the context of eutectic structures, the sharing of the Si element plays a crucial role. When the eutectic solution containing Si transforms into an amorphous structure, the remaining elements tend to form a solid solution, ultimately leading to the creation of an amorphous alloy composite that incorporates both amorphous and crystalline structures. Given this complexity, the phase selection prediction for the $Zr_{17}Ta_{16}Ti_{19}Nb_{22}Si_{26}$ alloy can indeed lead to both true positive and false positive examples.

The learning model's prediction of Zr−Hf−Ti−Cu−Ni high-entropy amorphous alloy with an equal atomic ratio in both the AM and IM phases indicates that both have relatively high predicted values of 9.31 and 11.41, respectively, which are greater than the threshold of 7.5. This suggests that both phases are likely to form in the alloy. Regarding the composition of ZrHfTiCuNi high-entropy amorphous alloy, Zr, Hf, and Ti are known to have a strong tendency to form solid solutions due to their similar atomic sizes and electronic structures. When Zr, Hf, and Ti easily form eutectic clusters with Cu and Ni elements, the formation of amorphous alloys is facilitated during the cooling process of the alloy solution. The critical size for the formation ability of Zr−Hf−Ti−Cu−Ni high-entropy amorphous alloy is 4 mm. When the cooling rate of the alloy solution is lower than the critical cooling rate, the alloy solution tends to form amorphous composites containing crystals [26]. Therefore, ZrHfTiCuNi alloy is prone to form amorphous composites with crystal structures. In the context of learning prediction, the predicted values of AM and IM phase selection may show true positive or false positive examples. As a result, both true positive and false positive examples are necessary in the phase selection prediction of the ANN model in order to accurately predict amorphous composites.

3.3 Prediction of AM and IM phase selection in amorphous alloy composites

To verify the accuracy of the learning model in predicting phase selection for AACs, a training set consisting of 330 alloys was used, while the test set comprised 30 AACs listed in Table 2. The learning model performed AM and IM phase selection predictions on these 30 alloys. Table 2 presents the three characteristic parameters of the 30 alloys and the sum of the 15 predicted values for AM and IM (P_{am} and P_{im}) phase selection predictions. In the case of AM phase selection predictions for the 30 alloys, all P_{am} values were found to be not less than 11.53. This indicates that the phase predictions for these 30 alloys are true positive examples, as depicted in Fig. 6(a). For IM phase selection prediction, 8 alloys had P_{im} values below 7.5, suggesting that these 8 alloys were true negative examples. However, the remaining 22 alloys were false positive examples, resulting in a precision of 73.3%. Therefore, the current learning model also demonstrates a high P_c(IM) value for the 30 AACs.

When the number of prediction times is different, it is necessary to normalize the sum of predicted values. The expressions for normalizing the sum of predicted values selected by AM and IM phases (N_{am} and N_{im}) are as follows:

$$N_{am} = 1 - \frac{1}{n}\sum_{i}^{n} P_i \tag{5a}$$

$$N_{im} = 1 - \frac{1}{n}\sum_{i}^{n} P_i \tag{5b}$$

where n represents the number of predictions, and P_i represents the predicted value for the selection of phase i. When the values of N_{am} and N_{im} are closer to 1, the activation of neural units for phase selection is weaker, resulting in a smaller probability for the alloy to form that particular phase. When the normalization value is greater than 0.5, the prediction for phase selection is a true negative or false negative example. On the other hand, when the normalized value approaches 0, the selected prediction is a true positive or false positive example. Figure 6(b) illustrates the normalized values of the sum of 15 predicted values in AM and IM phase selection predictions for the 30 AACs. Among these, 8 alloys have normalized values greater than 0.5, indicating that these alloys represent true negative examples in the IM phase-selection prediction. On the other hand, the remaining 22 alloys demonstrate true positive and false positive examples in the AM and IM phase-selection predictions, respectively.

In Table 2, it is observed that the addition of trace amounts of Nb element weakens the glass forming ability of Cu−Hf−Ti−Nb quaternary alloy, which is known for its good glass forming ability [27]. This is evident from the decrease in P_{am}

Table 2 Three characteristic parameters of 30 AACs, sum of 15 predicted values (P_{am} and P_{im}) in AM and IM phase selection prediction, as well as normalized values (N_{am} and N_{im}) of predicted values

Alloy	δ	$\Delta\chi$	S_{id}/(J·mol^{-1}·K^{-1})	P_{am}	N_{am}	P_{im}	N_{im}
$[(Co_{0.7}Fe_{0.3})_{0.75}B_{0.2}Si_{0.05}]_{96}Nb_4$	14.97	0.09	10.54	13.87	0.075	15.79	0.052
$[(Co_{0.9}Fe_{0.1})_{0.75}B_{0.2}Si_{0.05}]_{96}Nb_4$	15.01	0.09	8.83	15.19	0.013	15.82	0.054
$[(Co_{0.6}Fe_{0.4})_{0.75}B_{0.2}Si_{0.05}]_{96}Nb_4$	14.96	0.09	10.91	13.30	0.113	15.67	0.044
$[(Co_{0.8}Fe_{0.2})_{0.75}B_{0.2}Si_{0.05}]_{96}Nb_4$	14.99	0.09	9.88	14.62	0.025	15.93	0.062
$(Cu_{0.6}Hf_{0.25}Ti_{0.15})_{98}Nb_2$	9.37	0.26	8.46	14.13	0.058	3.66	0.756
$(Cu_{0.6}Hf_{0.25}Ti_{0.15})_{96}Nb_4$	9.28	0.26	8.88	14.02	0.065	4.07	0.729
$(Cu_{0.6}Hf_{0.25}Ti_{0.15})_{94}Nb_6$	9.19	0.25	9.22	13.72	0.085	4.72	0.685
$(Cu_{0.6}Hf_{0.25}Ti_{0.15})_{92}Nb_8$	9.09	0.25	9.49	13.46	0.101	5.00	0.667
$Fe_{36}Co_{36}B_{19.2}Si_{4.8}Nb_4$	14.94	0.09	11.03	13.10	0.126	15.62	0.041
$[(Fe_{0.5}Co_{0.5})_{0.75}B_{0.2}Si_{0.05}]_{96}Nb_4$	14.94	0.09	11.03	13.10	0.126	15.62	0.041
$Fe_{56.8}B_{24}Co_{14.2}Nb_5$	16.53	0.12	9.07	14.93	0.004	13.40	0.107
$[(Fe_{0.6}Co_{0.4})_{0.75}B_{0.2}Si_{0.05}]_{96}Nb_4$	14.92	0.10	10.91	13.58	0.094	14.91	0.006
$[(Fe_{0.7}Co_{0.3})_{0.75}B_{0.2}Si_{0.05}]_{96}Nb_4$	14.90	0.10	10.54	14.13	0.058	15.08	0.005
$Fe_{72}B_{20}Nb_4Si_4$	15.11	0.10	6.78	14.31	0.046	13.62	0.092
$Fe_{55.8}B_{24}Co_{14.2}Nb_6$	16.66	0.11	9.26	14.61	0.026	14.22	0.052
$(Fe_{0.75}B_{0.15}Si_{0.1})_{98}Nb_2$	12.94	0.08	6.77	13.08	0.128	13.67	0.088
$(Fe_{0.8}Co_{0.2})_{71}B_{23}Nb_6$	16.36	0.11	9.19	14.83	0.011	14.38	0.041
$Fe_{75.71}B_{14.29}Si_{7.14}Zr_{2.86}$	13.73	0.12	6.48	13.82	0.079	10.89	0.274
$Fe_{73}B_{20}Nb_4Hf_3$	16.12	0.14	6.53	14.51	0.033	9.26	0.383
$Fe_{72.8}B_{16}Si_8Zr_{3.2}$	14.51	0.12	6.96	14.64	0.024	11.97	0.202
$Zr_{48}Be_{18}Cu_{14}Ni_{12}Nb_8$	13.74	0.24	11.58	14.68	0.022	4.49	0.701
$Zr_{48}Be_{24}Cu_{12}Fe_8Nb_8$	14.44	0.21	11.25	14.76	0.016	5.56	0.629
$Fe_{67}B_{22}Y_6Mo_5$	19.89	0.19	7.65	14.24	0.051	2.01	0.866
$(Fe_{0.75}B_{0.15}Si_{0.1})_{99}Nb_1$	12.84	0.08	6.48	12.53	0.164	13.28	0.115
$Ni_{42}Zr_{20.5}Ti_{20}Al_8Cu_5Si_{4.5}$	10.80	0.24	12.49	11.53	0.231	7.76	0.482
$Ni_{42}Zr_{22.5}Ti_{19}Al_8Cu_5Si_{3.5}$	10.86	0.24	12.34	12.05	0.197	7.50	0.501
$Ni_{59}Zr_{20}Ti_{16}Si_5$	11.27	0.24	8.95	15.15	0.010	2.83	0.811
$Ni_{42}Zr_{21.5}Ti_{20}Al_8Cu_5Si_{3.5}$	10.77	0.24	12.35	11.86	0.209	7.56	0.496
$(Ni_{0.75}B_{0.2}Si_{0.05})_{96}Nb_4$	14.84	0.08	6.88	14.05	0.064	14.87	0.009
$[(Ni_{0.9}Fe_{0.1})_{0.75}B_{0.2}Si_{0.05}]_{96}Nb_4$	14.84	0.09	8.83	15.16	0.010	15.78	0.052

values from 14.13 to 13.46, and the corresponding increase in N_{am} values from 0.058 to 0.101. Additionally, although the P_{im} values remain below 7.5, they increase with the increase in Nb content, indicating a higher probability of IM phase formation. Therefore, a higher Nb content leads to a decrease in the content of amorphous structure in AACs, and an increase in the content of intermetallic compounds, which is consistent with the experimental findings [27]. In fact, this also provides a new method for machine learning to predict the amorphous formation ability of alloys. The enthalpy changes of mixing between Cu−Nb, Hf−Nb, and Ti−Nb atomic pairs are 3, 4, and 2 kJ/mol, respectively [28]. When the enthalpy change of mixing between atomic pairs is positive, the formation of solid solution alloys is similar. Therefore, with a higher Nb content, the probability

of forming solid solution increases, inhibiting the formation of amorphous structures in eutectic clusters containing Cu−Hf and Cu−Ti atomic pairs. As the Nb content increases, the glass formation ability of the alloy decreases, while the probability of crystal phase formation increases.

3.4 Prediction and experimental verification of AM and IM phases in some unknown AACs

To predict the formation probability of amorphous and crystalline phases in unknown AACs, AM and IM phase-selection predictions were conducted on 14 Ti−Cu−Ni−Zr−Hf alloys. The training set consisted of 330 alloys, while the test set comprised the 14 Ti−Cu−Ni−Zr−Hf alloys listed in Table 3. Table 3 presents the four parameter values of the alloys, the sum of predicted values (P_{am} and P_{im}), and the normalized values of predicted values (N_{am} and N_{im}) for the AM and IM phase selection. The element content of the alloy influences the phase selection, which subsequently affects the normalization value of the predicted values.

To determine the relationship between the content of each element and N_{am} and N_{im}, Fig. 7 illustrates the correlation between the molar fractions of Ti, Cu, Ni, Zr and Hf and N_{am} and N_{im}. In the prediction of AM phase selection, an increase

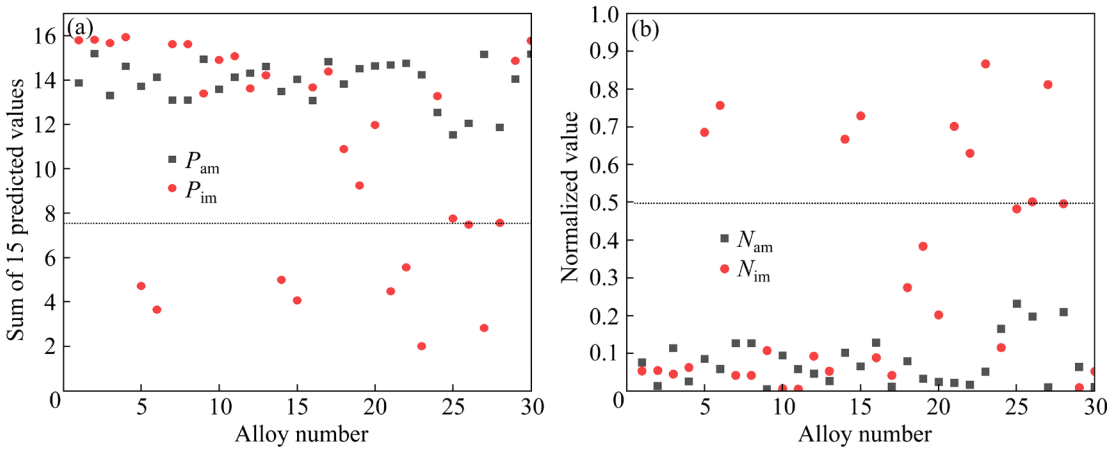

Fig. 6 Sum of 15 predicted values (a) and normalized values (b) in AM and IM phase selection predictions for 30 amorphous alloy composites

Table 3 Four characteristic parameters of 14 Ti−Cu−Ni−Zr−Hf alloys, sum of 15 predicted values (P_{am} and P_{im}) in AM and IM phase selection predictions, as well as normalized values (N_{am} and N_{im}) of predicted values

Alloy	d_c/mm	δ	$\Delta\chi$	S_{id}/(J·mol^{-1}·K^{-1})	P_{am}	N_{am}	P_{im}	N_{im}
$Ti_{26.5}Cu_{51.1}Ni_{6.4}Zr_{7.6}Hf_{8.4}$	<3	8.99	0.23	10.60	13.58	0.094	7.77	0.482
$Ti_{27.48}Cu_{49.64}Ni_{6.88}Zr_{7.6}Hf_{8.4}$	3	8.98	0.23	10.73	13.41	0.106	8.10	0.460
$Ti_{28.46}Cu_{48.18}Ni_{7.36}Zr_{7.6}Hf_{8.4}$	3	8.97	0.23	10.85	13.23	0.118	8.39	0.440
$Ti_{29.44}Cu_{46.72}Ni_{7.84}Zr_{7.6}Hf_{8.4}$	3[29]	8.96	0.23	10.97	13.02	0.132	8.68	0.422
$Ti_{30.42}Cu_{45.26}Ni_{8.32}Zr_{7.6}Hf_{8.4}$	4[29]	8.95	0.23	11.07	12.83	0.145	8.90	0.406
$Ti_{31.4}Cu_{43.8}Ni_{8.8}Zr_{7.6}Hf_{8.4}$	4[29]	8.94	0.23	11.17	12.62	0.159	9.12	0.392
$Ti_{32.38}Cu_{42.34}Ni_{9.28}Zr_{7.6}Hf_{8.4}$	4[29]	8.92	0.23	11.25	12.41	0.173	9.31	0.379
$Ti_{33.36}Cu_{40.88}Ni_{9.76}Zr_{7.6}Hf_{8.4}$	<3[29]	8.91	0.23	11.33	12.21	0.186	9.47	0.368
$Ti_{34.34}Cu_{39.42}Ni_{10.24}Zr_{7.6}Hf_{8.4}$	<3	8.89	0.23	11.40	11.99	0.201	9.63	0.358
$Ti_{35.32}Cu_{37.96}Ni_{10.72}Zr_{7.6}Hf_{8.4}$	<3	8.87	0.23	11.46	11.79	0.214	9.77	0.349
$Ti_{36.3}Cu_{36.5}Ni_{11.2}Zr_{7.6}Hf_{8.4}$	<3	8.85	0.23	11.51	11.61	0.226	9.88	0.341
$Ti_{37.28}Cu_{35.04}Ni_{11.68}Zr_{7.6}Hf_{8.4}$	<3	8.83	0.23	11.56	11.42	0.239	9.99	0.334
$Ti_{38.26}Cu_{33.58}Ni_{12.16}Zr_{7.6}Hf_{8.4}$	<3	8.81	0.23	11.59	11.27	0.249	10.07	0.329
$Ti_{39.24}Cu_{32.12}Ni_{12.64}Zr_{7.6}Hf_{8.4}$	<3	8.78	0.23	11.62	10.98	0.268	10.17	0.322

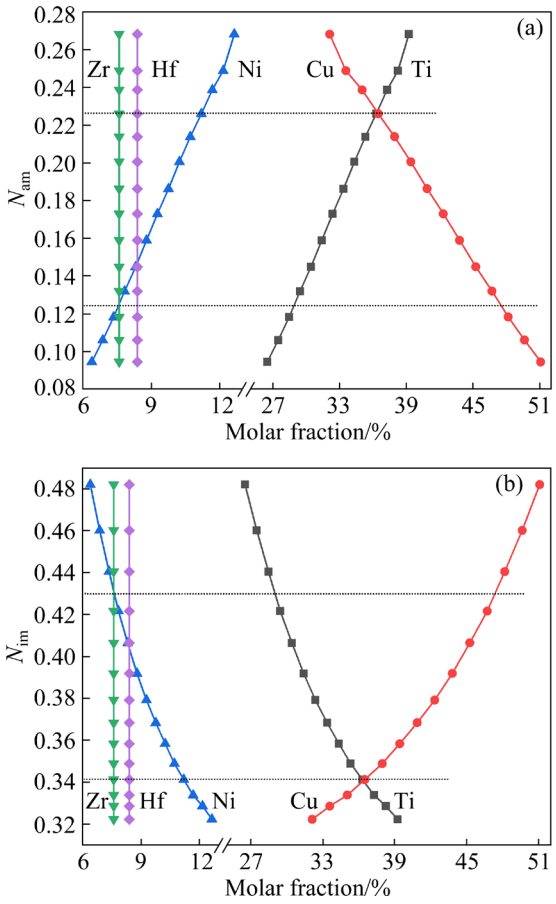

Fig. 7 Relationship between normalized values and element contents of 15 predicted values in AM (a) and IM (b) selection phases for 14 Ti−Cu−Ni−Zr−Hf alloys

in Ni and Ti contents leads to an increase in N_{am} value, indicating a decrease in the probability of AM phase formation. Conversely, an increase in Cu content results in a decrease in N_{am} value, indicating an increase in the probability of AM phase formation. From Fig. 6 and Table 3, it can be observed that when the Cu content exceeds 45.26 at.%, the critical sizes for the ability to form amorphous structures in the alloys reduce from 4 to 3 mm. Furthermore, with further increase in Cu content (>51.1 at.%), the critical sizes of the alloys become smaller than 3 mm. This means that the critical size of the amorphous forming ability of Ti−Cu−Ni−Zr−Hf alloys does not increase with an increase in Cu content. Moreover, the observed trend of glass forming ability under experimental conditions does not align with the predicted trend. The reason for this discrepancy lies in the fact that when the Cu content is high, the composition of the alloy deviates from the eutectic alloy composition. As a result, certain clusters containing Cu generate competitive crystal phases during the cooling process, which hampers the formation of the amorphous phase in the alloy.

According to the research on the Ti−Cu−Ni−Zr−Hf alloy system, there is a contradictory relationship between the Cu and Ti contents and the formation probability of the AM phase. To resolve this contradiction, in Fig. 7(a), the intersection point is identified where the contents of Cu and Ti atoms are equal, corresponding to a content of 36 at.% for both Cu and Ti. Similarly, the intersection point of the contents of Ni and Zr atoms is identified, which corresponds to a content of 7.56 at.% for both Ni and Zr. A dashed line is drawn parallel to the horizontal axis at these two intersection points. When the value of N_{am} is between the two dashed lines, that is, $0.125 \leq N_{am} \leq 0.226$, the formation probability of the AM phase is neither particularly large nor particularly small. When the value of N_{am} exceeds 0.226, indicating a Ti content greater than 36 at.%, the formation probability of the AM phase decreases. Conversely, when the value of N_{am} exceeds 0.125, indicating a Ti content less than 28.8 at.%, the formation probability of the AM phase increases. However, this contradicts the experimental values, as lower Ti content causes the alloy components to deviate from those of the eutectic alloy, resulting in the presence of clusters with lower Ti content in the alloy melt, which inhibits the ability of the alloy to form the amorphous phase during the cooling process.

To obtain amorphous alloy composites, it is necessary to determine the Zr and Hf contents. In the AM phase prediction, it is important to ensure that the Ti content is greater than 28.8 at.% but less than 36 at.%, the corresponding Cu content is greater than 36 at.% but less than 47.6 at.%, and the Ni content is greater than 7.56 at.% but less than 11.2 at.%. When the Ti, Cu, and Ni contents fall within the respective ranges, the formation probability of the AM phase is moderate, neither particularly high nor particularly low. This balanced probability favors the formation of both amorphous and crystalline phases in the composite material. Alloy melts are prone to form crystalline materials with amorphous structures, known as amorphous alloy composites. Figure 7(b) illustrates the normalized relationship between 15 predicted values and the element contents in the prediction of the IM phase for 14 Ti−Cu−Ni−Zr−Hf alloys. In the

prediction of IM phase selection, when the N_{im} value is less than 0.341 (corresponding to Ti content higher than 36.3 at.%), the likelihood of forming the IM phase is enhanced, which aligns with the XRD results shown in Fig. 8. Conversely, when the N_{im} value exceeds 0.43, the probability of IM phase formation diminishes. In the range of $0.341 \leq N_{im} \leq 0.43$, the formation probability of the IM phase neither significantly increases nor decreases. This means that both amorphous and crystalline phases coexist in the alloy structure, with corresponding Ti contents in the range of 28.8 at.%−36 at.%. Therefore, by utilizing the normalization of the predicted values selected for AM and IM phases, it becomes possible to determine the elemental composition of AACs.

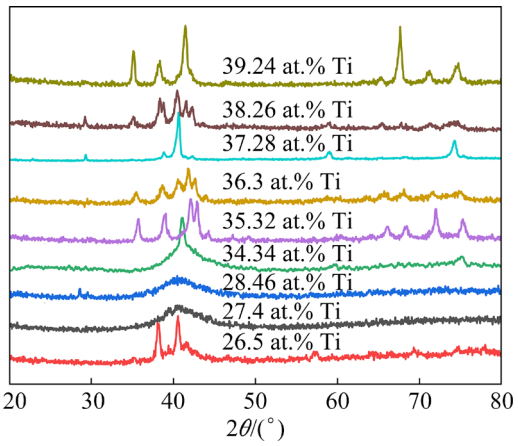

Fig. 8 XRD patterns of Ti−Cu−Ni−Zr−Hf alloys

3.5 Prediction and experimental validation of AM and IM phase selection in novel multiple-principal Ti−Cu−Ni−Hf alloys

To predict the specific components of novel multiple-principal Ti−Cu−Ni−Hf AACs, the AM and IM phase selections for 40 alloy compositions were predicted. Without using machine learning models for prediction, determining the composition of these 40 AACs would require extensive sample preparation and phase testing. This would result in significant labor and raw material costs. By utilizing machine learning methods to predict a smaller range of components, it is possible to save labor and raw material costs, thereby reducing the design time for new materials. The training set consisted of 330 alloys, while the test set comprised the 40 Ti−Cu−Ni−Hf alloys listed in Table 4.

Figure 9 illustrates the relationship between the N_{am} and N_{im} values of 40 alloys and the contents of alloy atoms. In the prediction of the AM phase, as the contents of Ti and Cu increase, the normalized value also increases, indicating a weakened probability of amorphous formation but an increased probability of crystal formation. Conversely, when the Ni and Hf contents increase, the normalized value decreases, suggesting an increased probability of amorphous formation but a decreased probability of crystal formation. Similar trends are observed in the prediction of the IM phase, which aligns with the findings from the AM phase prediction.

To obtain a composition range where the formation probability of amorphous or crystalline materials is neither significantly large nor small, the point of intersection between the Ti and Ni contents is selected, which is 32.7 at.%. At this point, a straight line parallel to the X-axis is drawn, intersecting with the Cu and Hf contents, to determine the contents of Cu and Hf (Cu: 16.4 at.% and Hf: 18.3 at.%). Similarly, the intersection point of Cu and Hf is selected, where the contents of Cu and Hf are 17.3 at.%, and a straight line is drawn to determine the contents of Ni and Hf (Ni: 30.9 at.% and Ti: 34.5 at.%). In Fig. 9(b), by using the same analytical method, one can obtain the range of contents of Ti, Cu, Ni, and Hf. Therefore, when the Ti content is between 32.7 at.% and 34.5 at.%, the Cu content is between 16.4 at.% and 17.3 at.%, the Ni content is between 30.9 at.% and 32.7 at.%, and the Hf content is between 17.3 at.% and 18.3 at.%, the probability of forming amorphous or crystalline structures in the alloy is neither particularly large nor small. Alloys within these ranges are more prone to form amorphous alloy composites.

To validate the machine learning model for predicting the amorphous and crystalline phases of Ti−Cu−Ni−Hf alloys, the experimental verification is conducted using four alloys: $Ti_{32}Cu_{16}Ni_{33.28}Hf_{18.72}$, $Ti_{34}Cu_{17}Ni_{31.36}Hf_{17.64}$, $Ti_{36}Cu_{18}Ni_{29.44}Hf_{16.56}$, and $Ti_{38}Cu_{19}Ni_{27.52}Hf_{15.48}$. The XRD patterns of these alloys with a diameter of 3 mm are shown in Fig. 10. The $Ti_{32}Cu_{16}Ni_{33.28}Hf_{18.72}$ and $Ti_{38}Cu_{19}Ni_{27.52}Hf_{15.48}$ alloys consist of crystalline phases, while the $Ti_{34}Cu_{17}Ni_{31.36}Hf_{17.64}$ and $Ti_{36}Cu_{18}Ni_{29.44}Hf_{16.56}$ alloys consist of both crystalline and amorphous phases. The composition of the four elements in $Ti_{32}Cu_{16}Ni_{33.28}Hf_{18.72}$ and $Ti_{38}Cu_{19}Ni_{27.52}Hf_{15.48}$ alloys falls within the predicted composition range for crystalline phases. Therefore,

Table 4 Three characteristic parameters of 40 Ti−Cu−Ni−Hf alloys, as well as normalized values (N_{am} and N_{im}) of sum of 15 predicted values in AM and IM phase selection prediction

Alloy	δ	$\Delta\chi$	S_{id}/(J·mol^{-1}·K^{-1})	N_{am}	N_{im}
$Ti_{40}Cu_{20}Ni_{25.6}Hf_{14.4}$	8.83	0.23	10.94	0.1467	0.1553
$Ti_{39.6}Cu_{19.8}Ni_{25.984}Hf_{14.616}$	8.86	0.23	10.96	0.1449	0.1552
$Ti_{39.2}Cu_{19.6}Ni_{26.368}Hf_{14.832}$	8.89	0.23	10.98	0.1431	0.1550
$Ti_{38.8}Cu_{19.4}Ni_{26.752}Hf_{15.048}$	8.93	0.23	11	0.1400	0.1559
$Ti_{38.4}Cu_{19.2}Ni_{27.136}Hf_{15.264}$	8.96	0.23	11.02	0.1383	0.1559
$Ti_{38}Cu_{19}Ni_{27.52}Hf_{15.48}$	8.99	0.23	11.03	0.1355	0.1574
$Ti_{37.6}Cu_{18.8}Ni_{27.904}Hf_{15.696}$	9.02	0.23	11.05	0.1339	0.1576
$Ti_{37.2}Cu_{18.6}Ni_{28.288}Hf_{15.912}$	9.06	0.23	11.06	0.1299	0.1602
$Ti_{36.8}Cu_{18.4}Ni_{28.672}Hf_{16.128}$	9.09	0.23	11.07	0.1272	0.1618
$Ti_{36.4}Cu_{18.2}Ni_{29.056}Hf_{16.344}$	9.12	0.23	11.08	0.1246	0.1636
$Ti_{36}Cu_{18}Ni_{29.44}Hf_{16.56}$	9.15	0.23	11.09	0.1220	0.1654
$Ti_{35.6}Cu_{17.8}Ni_{29.824}Hf_{16.776}$	9.19	0.24	11.1	0.1076	0.1702
$Ti_{35.2}Cu_{17.6}Ni_{30.208}Hf_{16.992}$	9.22	0.24	11.11	0.1054	0.1716
$Ti_{34.8}Cu_{17.4}Ni_{30.592}Hf_{17.208}$	9.25	0.24	11.11	0.1022	0.1747
$Ti_{34.4}Cu_{17.2}Ni_{30.976}Hf_{17.424}$	9.28	0.24	11.12	0.1000	0.1763
$Ti_{34}Cu_{17}Ni_{31.36}Hf_{17.64}$	9.31	0.24	11.12	0.0970	0.1795
$Ti_{33.6}Cu_{16.8}Ni_{31.744}Hf_{17.856}$	9.34	0.24	11.12	0.0939	0.1828
$Ti_{33.2}Cu_{16.6}Ni_{32.128}Hf_{18.072}$	9.38	0.24	11.13	0.0910	0.1857
$Ti_{32.8}Cu_{16.4}Ni_{32.512}Hf_{18.288}$	9.41	0.24	11.13	0.0881	0.1892
$Ti_{32.4}Cu_{16.2}Ni_{32.896}Hf_{18.504}$	9.44	0.24	11.12	0.0843	0.1944
$Ti_{32}Cu_{16}Ni_{33.28}Hf_{18.72}$	9.47	0.24	11.12	0.0816	0.1980
$Ti_{31.6}Cu_{15.8}Ni_{33.664}Hf_{18.936}$	9.50	0.24	11.12	0.0789	0.2017
$Ti_{31.2}Cu_{15.6}Ni_{34.048}Hf_{19.152}$	9.53	0.24	11.11	0.0753	0.2072
$Ti_{30.8}Cu_{15.4}Ni_{34.432}Hf_{19.368}$	9.56	0.24	11.11	0.0728	0.2111
$Ti_{30.4}Cu_{15.2}Ni_{34.816}Hf_{19.584}$	9.59	0.24	11.1	0.0694	0.2168
$Ti_{30}Cu_{15}Ni_{35.2}Hf_{19.8}$	9.62	0.25	11.09	0.0618	0.2419
$Ti_{29.6}Cu_{14.8}Ni_{35.584}Hf_{20.016}$	9.65	0.25	11.08	0.0588	0.2479
$Ti_{29.2}Cu_{14.6}Ni_{35.968}Hf_{20.232}$	9.68	0.25	11.07	0.0559	0.2540
$Ti_{28.8}Cu_{14.4}Ni_{36.352}Hf_{20.448}$	9.71	0.25	11.06	0.0531	0.2603
$Ti_{28.4}Cu_{14.2}Ni_{36.736}Hf_{20.664}$	9.74	0.25	11.04	0.0495	0.2688
$Ti_{28}Cu_{14}Ni_{37.12}Hf_{20.88}$	9.77	0.25	11.03	0.0468	0.2753
$Ti_{27.6}Cu_{13.8}Ni_{37.504}Hf_{21.096}$	9.80	0.25	11.01	0.0435	0.2843
$Ti_{27.2}Cu_{13.6}Ni_{37.888}Hf_{21.312}$	9.83	0.25	11	0.0409	0.2911
$Ti_{26.8}Cu_{13.4}Ni_{38.272}Hf_{21.528}$	9.86	0.25	10.98	0.0379	0.3003
$Ti_{26.4}Cu_{13.2}Ni_{38.656}Hf_{21.744}$	9.89	0.25	10.96	0.0347	0.3098
$Ti_{26}Cu_{13}Ni_{39.04}Hf_{21.96}$	9.92	0.25	10.94	0.0318	0.3196
$Ti_{25.6}Cu_{12.8}Ni_{39.424}Hf_{22.176}$	9.95	0.25	10.92	0.0289	0.3295
$Ti_{25.2}Cu_{12.6}Ni_{39.808}Hf_{22.392}$	9.98	0.25	10.89	0.0255	0.3424
$Ti_{24.8}Cu_{12.4}Ni_{40.192}Hf_{22.608}$	10.01	0.25	10.87	0.0228	0.3529
$Ti_{24.4}Cu_{12.2}Ni_{40.576}Hf_{22.824}$	10.04	0.26	10.84	0.0199	0.4148

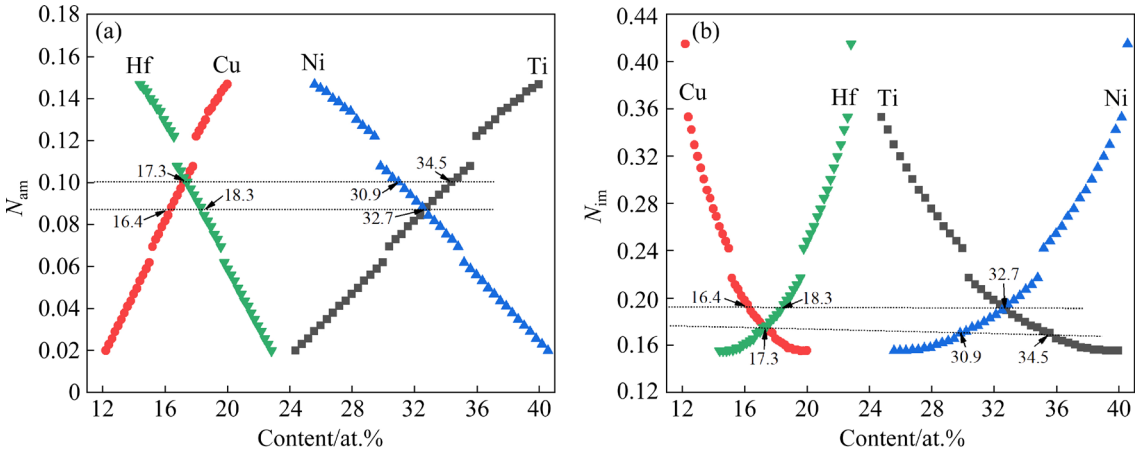

Fig. 9 Relationship between normalized values and element contents of 40 alloys in AM (a) and IM (b) phase selection prediction

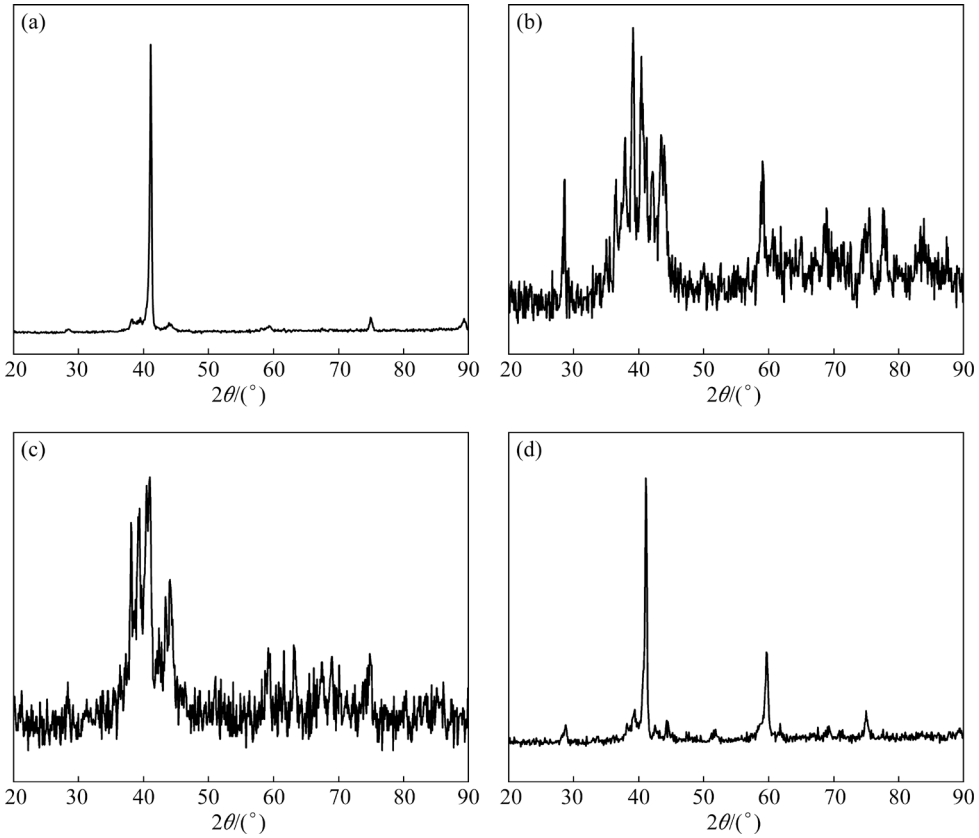

Fig. 10 XRD patterns of new multiple-principal Ti−Cu−Ni−Hf alloys with diameter of 3 mm: (a) $Ti_{32}Cu_{16}Ni_{33.28}Hf_{18.72}$; (b) $Ti_{34}Cu_{17}Ni_{31.36}Hf_{17.64}$; (c) $Ti_{36}Cu_{18}Ni_{29.44}Hf_{16.56}$; (d) $Ti_{38}Cu_{19}Ni_{27.52}Hf_{15.48}$ alloys

these alloys are classified as crystalline. On the other hand, the composition of the four elements in the $Ti_{34}Cu_{17}Ni_{31.36}Hf_{17.64}$ alloy lies within the predicted composition range for both amorphous and crystalline phases, indicating a coexistence of these two phases in the alloy. However, the $Ti_{36}Cu_{18}Ni_{29.44}Hf_{16.56}$ alloy has a composition that is close to the predicted composition range as shown in Table 5. Consequently, the $Ti_{34}Cu_{17}Ni_{31.36}Hf_{17.64}$ and $Ti_{36}Cu_{18}Ni_{29.44}Hf_{16.56}$ alloys can be considered as good amorphous and crystalline alloys, closely resembling the predicted composition ranges.

To better illustrate the presence of amorphous structures in the microstructure of $Ti_{34}Cu_{17}Ni_{31.36}Hf_{17.64}$ and $Ti_{36}Cu_{18}Ni_{29.44}Hf_{16.56}$ alloys, Fig. 11 displays the HRTEM and corresponding Fourier transform images of the mentioned alloys. In the HRTEM images, a coexistence of amorphous and

Table 5 Range of predicted molar fraction for amorphous and crystalline phases of 40 Ti−Cu−Ni−Hf alloys, and molar fraction of four elements in four experimental alloys

Range	Content/at.%			
	Ti	Cu	Ni	Hf
R_p (AM+IM)	32.7−34.5	16.4−17.3	30.9−32.7	17.3−18.3
R_e (AM+IM)	34, 36	17, 18	31.36, 29.44	17.64, 16.56
R_p (IM)	<32.7, >34.5	<16.4, >17.3	<30.9, >32.7	<17.3, >18.3
R_e (IM)	32, 38	16, 19	27.52, 33.28	15.48, 18.72

R_p is range of predicted values; R_e is range of experimental values

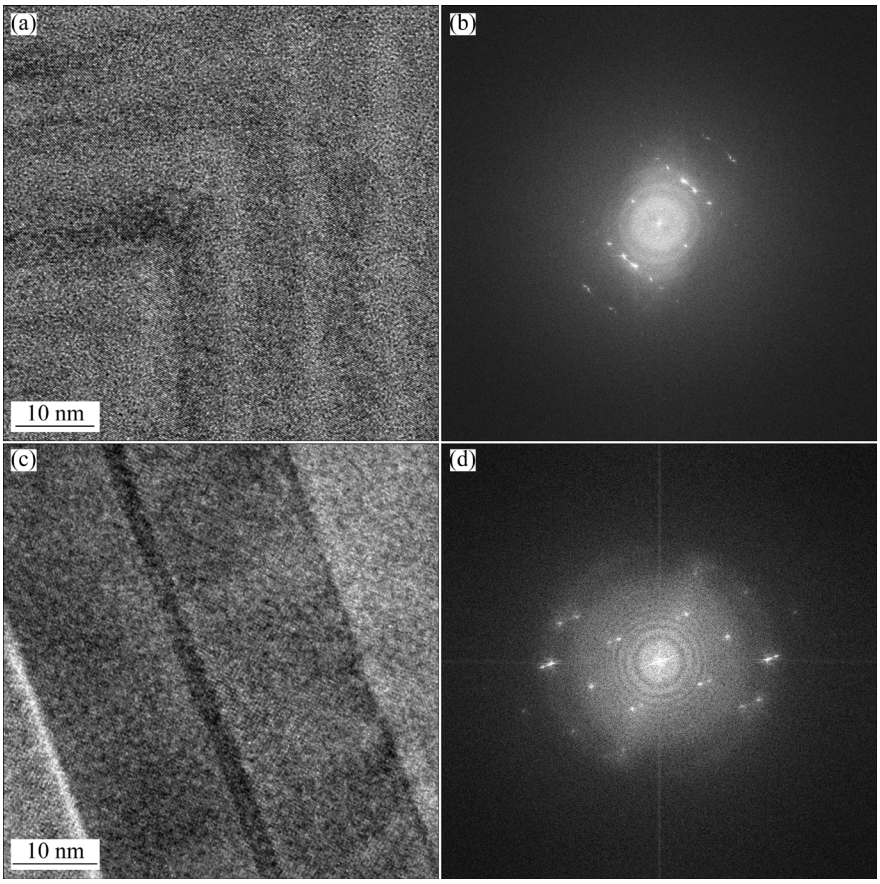

Fig. 11 HRTEM (a, c) and Fourier transform (b, d) images of $Ti_{34}Cu_{17}Ni_{31.36}Hf_{17.64}$ (a, b) and $Ti_{36}Cu_{18}Ni_{29.44}Hf_{16.56}$ (c, d)

crystalline structures can be observed. Fourier transform was performed on the HRTEM images, resulting in the appearance of halos representing the amorphous structure and diffraction spots representing the crystalline structure. Consequently, the microstructure shown in the HRTEM images is consistent with the results obtained from XRD.

4 Conclusions

(1) In terms of phase formation probability in AACs, ANN outperforms the KNN model based on prediction accuracies, R values, and MSE values. Therefore, the ANN algorithm is suitable for predicting the phase selection of amorphous alloy composite materials.

(2) An expression is defined to normalize the sum of predicted values selected by AM and IM phases as N_{am} and N_{im}, respectively. When the values of N_{am} and N_{im} approach 1, weaker activation of neural units for phase selection will occur, resulting in a lower probability for the alloy to form that particular phase.

(3) In Ti−Cu−Ni−Zr−Hf alloys, when the normalized N_{im} value is greater than 0.43, the probability of IM phase formation will decrease.

When $0.341 \leq N_{im} \leq 0.43$, both amorphous and crystalline phases will be present in the alloy structure, with the corresponding Ti content ranging from 28.8 at.% to 36 at.%.

(4) For the novel multi-principal Ti−Cu−Ni−Hf alloys, when the Ti content ranges from 32.7 at.% to 34.5 at.%, Cu content ranges from 16.4 at.% to 17.3 at.%, Ni content ranges from 30.9 at.% to 32.7 at.%, and Hf content ranges from 17.3 at.% to 18.3 at.%, alloys within these ranges will be prone to form amorphous alloy composites.

(5) Based on the results of XRD and HRTEM analysis, the $Ti_{34}Cu_{17}Ni_{31.36}Hf_{17.64}$ and $Ti_{36}Cu_{18}Ni_{29.44}Hf_{16.56}$ alloys exhibit good amorphous alloy composites, which are consistent with the predicted amorphous alloy composition.

CRediT authorship contribution statement

Lin WANG: Conceptualization, Investigation, Formal analysis, Writing − Original draft; **Pei-you LI:** Conceptualization, Resources, Supervision, Writing − Review & editing; **Wei ZHANG:** Conceptualization, Investigation; **Xiao-ling FU**: Conceptualization, Investigation, Formal analysis; **Fang-yi WAN:** Formal analysis; **Yong-shan WANG:** Experimental guidance, Formal analysis; **Lin-sen SHU:** Experimental guidance, Funding acquisition; **Long-quan YONG:** Algorithm model guidance.

Declaration of competing interest

The authors declare that they have no known competing financial interests or personal relationships that could have appeared to influence the work reported in this paper.

Acknowledgments

The work was supported by the National Natural Science Foundation of China (No. 51601019), the Guangdong Basic and Applied Basic Research Foundation, China (No. 2022A1515010233), the Key Project of Shaanxi Province of Qinchuangyuan “Scientist and Engineer” Team Construction, China (No. 2023KXJ-123), and the Natural Science Foundation of Shaanxi Province, China (No. 2024JC-YBMS-014).

Data availability

The dataset used to generate the results in this work are available at https://github.com/amorphous-alloy-composites.

Code availability

The codes pertaining to the current work are available at https://github.com/amorphous-alloy-composites.

Supplementary materials

Supplementary materials in this paper can be found at: http://tnmsc.csu.edu.cn/download/12-p1543-2023-0998-Supplementary_Materials.pdf.

References

[1] WANG Shen, LI Da, XIONG Jun. Prediction of elastic properties of face-centered cubic high-entropy alloys by machine learning [J]. Transactions of Nonferrous Metals Society of China, 2023, 33: 518−530.

[2] OSMAN H, LIU Lin. Additive manufacturing of high-entropy alloy composites: A review [J]. Transactions of Nonferrous Metals Society of China, 2023, 33: 1−24.

[3] ZHANG Hui-ran, HU Rui, LIU Xi, LI Sheng-zhou, ZHANG Guang-jie, QIAN Quan, DING Guang-tai, DAI Dong-bo. An end-to-end machine learning framework exploring phase formation for high entropy alloys [J]. Transactions of Nonferrous Metals Society of China, 2023, 33: 2110−2120.

[4] AYDIN F, DURGUT R. Estimation of wear performance of AZ91 alloy under dry sliding conditions using machine learning methods [J]. Transactions of Nonferrous Metals Society of China, 2021, 31: 125−137.

[5] ZHANG Wei, LI Pei-you, WANG Lin, FU Xiao-ling, WAN Fang-yi, WANG Yong-shan, SHU Lin-sen, YONG Long-quan. Prediction of the yield strength of as-cast alloys using the random forest algorithm [J]. Materials Today Communications, 2024, 38: 108520.

[6] ISLAM N, HUANG W J, ZHUANG H L. Machine learning for phase selection in multi-principal element alloys [J]. Computational Materials Science, 2018, 150: 230−235.

[7] HOU Shuai, SUN Meng-yue, BAI Mei-juan, LIN Dong, LI Yu-jiao, LIU Wei-wei. A hybrid prediction frame for HEAs based on empirical knowledge and machine learning [J]. Acta Materialia, 2022, 228: 117742.

[8] ZHOU Zi-qing, ZHOU Ye-ju, HE Quan-feng, DING Zhao-yi, LI Fu-cheng, YANG Yong. Machine learning guided appraisal and exploration of phase design for high entropy alloys [J]. NPJ Computational Materials, 2019, 5: 128.

[9] LI Xin, SHAN Guang-cun, ZHANG Ji-liang, SHEK Chan-hung. Accelerated design for magnetic high entropy alloys using data-driven multi-objective optimization [J]. Journal of Materials Chemistry C, 2022, 10: 17291−17302.

[10] LI Xin, SHAN Guang-cun, ZHAO Hong-bin, SHEK Chan-hung. Domain knowledge aided machine learning method for properties prediction of soft magnetic metallic glasses [J]. Transactions of Nonferrous Metals Society of China, 2023, 33: 209−219.

[11] REN Bai-yu, LONG Zhi-lin, DENG Rui-jie. A new criterion for predicting the glass-forming ability of alloys based on machine learning [J]. Computational Materials Science, 2021, 189: 110259.

[12] WEN Cheng, ZHANG Yan, WANG Chang-xin, XUE De-zhen, BAI Yang, ANTONOV S, DAI Lan-hong, LOOKMAN T, SU Yan-jing. Machine learning assisted design of high entropy alloys with desired property [J]. Acta Materialia, 2019, 170: 109−117.

[13] ZHOU Zhi-hua. Machine learning [M]. Beijing: Tsinghua University Press, 2016. (in Chinese)

[14] ARAI K, KAPOOR S, BHATIA R. Intelligent systems and applications [C]//Proceedings of the 2020 Intelligent Systems Conference (IntelliSys). Cham: Springer, 2021.
[15] AWAD M, KHANNA R. Support vector regression [J]. Efficient Learning Machines, 2015, 27: 67−80.
[16] WU Qing-feng, WANG Zhi-jun, HU Xiao-bing, ZHENG Tao, YANG Zhong-sheng, HE Feng, LI Jun-jie, WANG Jin-cheng. Uncovering the eutectics design by machine learning in the Al−Co−Cr−Fe−Ni high entropy system [J]. Acta Materialia, 2020, 182: 278−286.
[17] HUANG Wen-jiang, MARTIN P, ZHUANG H L. Machine-learning phase prediction of high-entropy alloys [J]. Acta Materialia, 2019, 169: 225−236.
[18] ZHANG Yan, WEN Cheng, WANG Chang-xin, ANTONOV S, XUE De-zhen, BAI Yang, SU Yan-jing. Phase prediction in high entropy alloys with a rational selection of materials descriptors and machine learning models [J]. Acta Materialia, 2020, 185: 528−539.
[19] WANG Lin, LI Pei-you, ZHANG Wei, WAN Fang-yi, WU Jun-xia, YONG Long-quan, LIU Xiao-di. Prediction of phase selection of amorphous alloys and high entropy alloys by artificial neural network [J]. Computational Materials Science, 2023, 223: 112129.
[20] COVER T M, HART P E. Nearest neighbor pattern classification [J]. IEEE Transactions on information Theory, 1967, 13: 21−27.
[21] LEI Ming. Machine learning and application [M]. Beijing: Tsinghua University Press, 2018. (in Chinese)
[22] RUMELHART D E, MCCLELLAND J L. Learning internal representations by error propagation [M]. Cambridge: MIT Press, 1987.
[23] MOHAMMED J Z, WAGNER M. Data mining and machine learning: fundamental concepts and algorithms [M]. 2nd ed. Cambridge, UK: Cambridge University Press, 2020.
[24] ZHANG Wei, LI Pei-you, WANG Lin, WAN Fang-yi, WU Jun-xia, YONG Long-quan. Explaining of prediction accuracy on phase selection of amorphous alloys and high entropy alloys using support vector machines in machine learning [J]. Materials Today Communications, 2023, 35: 105694.
[25] YANG T H, HUANG R T, WU C A, CHEN F R, GAN J Y, YEH J W, NARAYAN J. Effect of annealing on atomic ordering of amorphous ZrTaTiNbSi alloy [J]. Applied Physics Letters, 2009, 95: 241905.
[26] MA Li-qun, WANG Li-min, ZHANG Tao, INOUE A. Bulk glass formation of Ti−Zr−Hf−Cu−M (M=Fe, Co, Ni) Alloys [J]. Materials Transactions, 2002, 43: 277−280.
[27] YUAN Zi-zhou, BAO Shi-lei, LU Ye, ZHANG Da-peng, YAO Lin. A new criterion for evaluating the glass-forming ability of bulk glass forming alloys [J]. Journal of Alloys and Compounds, 2008, 459: 251−260.
[28] TAKEUCHI A, INOUE A. Classification of bulk metallic glasses by atomic size difference, heat of mixing and period of constituent elements and its application to characterization of the main alloying element [J]. Materials Transactions, 2005, 46: 2817−2829.
[29] LI Pei-you, WANG Gang, DING Ding, SHEN Jun. Glass forming ability, thermodynamics and mechanical properties in the new Ti−Cu−Ni−Zr−Hf bulk metallic glasses [J]. Materials & Design, 2014, 53: 145−151.

基于人工神经网络模型的多主元非晶合金复合材料的相选择预测和成分确定

王 琳[1]，李培友[1]，张 薇[1]，付小玲[2]，万方义[3]，王永善[1]，舒林森[4]，雍龙泉[5]

1. 陕西理工大学 材料科学与工程学院，汉中 723001；
2. 广东工业大学 材料与能源学院，广州 510006；
3. 西北工业大学 航空学院，西安 710071；
4. 陕西理工大学 机械工程学院，汉中 723001；
5. 陕西理工大学 数学与计算机学院，汉中 723001

摘 要：用 *k*-近邻算法(KNN)和人工神经网络算法(ANN)对相形成概率进行预测，并用 ANN 模型预测未知的 40 种非晶合金复合材料(AACs)中 Ti、Cu、Ni 和 Hf 的组分范围。通过 X 射线衍射仪(XRD)和高分辨透射电镜(HRTEM)对预测合金进行实验验证。ANN 模型对 AM 和 IM 相的预测精度分别为 93.12%和 85.16%；KNN 模型对 AM 相和 IM 相的预测精度分别为 93%和 84%。当 Ti、Cu、Ni 和 Hf 的含量分别为 32.7%~34.5%、16.4%~17.3%、30.9%~32.7%和 17.3%~18.3% (摩尔分数)时更易形成 AACs。根据 XRD 和 HRTEM 实验结果，$Ti_{34}Cu_{17}Ni_{31.36}Hf_{17.64}$ 和 $Ti_{36}Cu_{18}Ni_{29.44}Hf_{16.56}$ 合金是较好的 AACs，与预测的非晶合金组分基本一致。

关键词：多主元非晶合金复合材料；Ti−Cu−Ni−Hf；相选择；人工神经网络；机器学习

(Edited by Wei-ping CHEN)